Design of a Passive Vertical Takeoff and Landing Aquatic UAV

Richard-Alexandre Peloquin, Dominik Thibault, and Alexis Lussier Desbiens

***Abstract*—With the goal of extending unmanned aerial vehicles mission duration, a solar recharge strategy is envisioned with lakes as preferred charging and standby areas. The Sherbrooke University Water-Air VEhicle (SUWAVE) concept developed is able to takeoff and land vertically on water. The physical prototype consists of a wing coupled to a rotating center body that minimizes the added components with a passive takeoff maneuver. A dynamic model of takeoff, validated with experimental results, serves as a design tool. The landing is executed by diving, without requiring complex control or wing folding. Structural integrity of the wing is confirmed by investigating the accelerations at impact. A predictive model is developed for various impact velocities. The final prototype has executed multiple repeatable takeoffs and has succeeded in completing full operation cycles of flying, diving, floating, and taking off.**

***Index Terms*—Aerial robotics, biologically-inspired robots, marine robotics.**

I. Introduction

EXISTING UAVs present a trade off between large UAVs that can fly for numerous hours and smaller platforms severely limited in their operating duration. To extend the mission duration of small UAVs, one could use solar panels. However, solar panels are not sufficient at small scale to enable continuous flight [1] and landing is required to recharge with minimum energy consumption before flight can be resumed. Numerous teams have created small drones that can land or perch in various locations as vertical walls, wires and moving vehicles [2]–[6]. However, finding suitable landing locations in realistic environment, without the use of processing intensive and heavy sensors (e.g., camera, lidar), remains a challenge. In many locations around the world, lakes represent a safe landing area for small UAVs as their locations are well known and their surface is smooth with little to no obstacles. A country like Canada has approximately 9% of its 10 million km^2 covered by lakes that see limited human activities [7]. Preliminary calculation based on hydrographic surveys [8] revealed that a flight range of only 20 km is necessary to traverse Quebec from north to south (1900 km) when traveling from lake to lake.

Fig. 1. Time lapse of SUWAVE's vertical takeoff sequence.

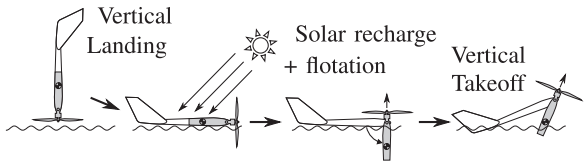

Fig. 2. Proposed concept for the vertical takeoff

Seaplanes [9]–[12] are often used as aquatic-aerial vehicles but they present challenges as they are scaled down [13]. Takeoff and landing are difficult in waves at smaller size. Also, the high wing and center of mass, along with the decreased wing loading of small UAVs, make them highly sensitive to capsize. Capsizing is an unacceptable failure mode for any long term operations. Aquatic quadrotors [14]–[17] are also used and present the advantage of vertical takeoff and landing (VTOL) capabilities. However, their range remains limited when compared to fixed wings. Quadplanes, a hybrid between quadrotors and fixed wing aircrafts, enable both VTOL and long endurance. However, the motors required for vertical thrust are not used in horizontal flight, resulting in dead weight and drag.

From these observations, some functional requirements are proposed and serve as guidelines for the design of a new type of aquatic UAV:

1) float stably on water
2) fixed wing for long endurance
3) large wing area for solar recharge
4) ability to right itself in the unlikely even of a capsize

Manuscript received September 10, 2016; accepted November 7, 2016. Date of publication December 1, 2016; date of current version December 26, 2016. This paper was recommended for publication by Associate Editor S. Nuske and Editor J. Roberts upon evaluation of the reviewers' comments.

The authors are with the Createk Design Lab, Université de Sherbrooke, Sherbrooke, QC J1K 2R1, Canada (e-mail: ra.peloquin@usherbrooke.ca; dominik.thibault@usherbrooke.ca; alexis.lussier.desbiens@usherbrooke.ca).

This letter has supplementary downloadable material available at http://ieeexplore.ieee.org The Supplementary Materials contain a video showing the aquatic UAV performing takeoff, flight, righting and landing maneuvers as described in the paper. This material is 40 MB in size.

Color versions of one or more of the figures in this letter are available online at http://ieeexplore.ieee.org.

Digital Object Identifier 10.1109/LRA.2016.2633623

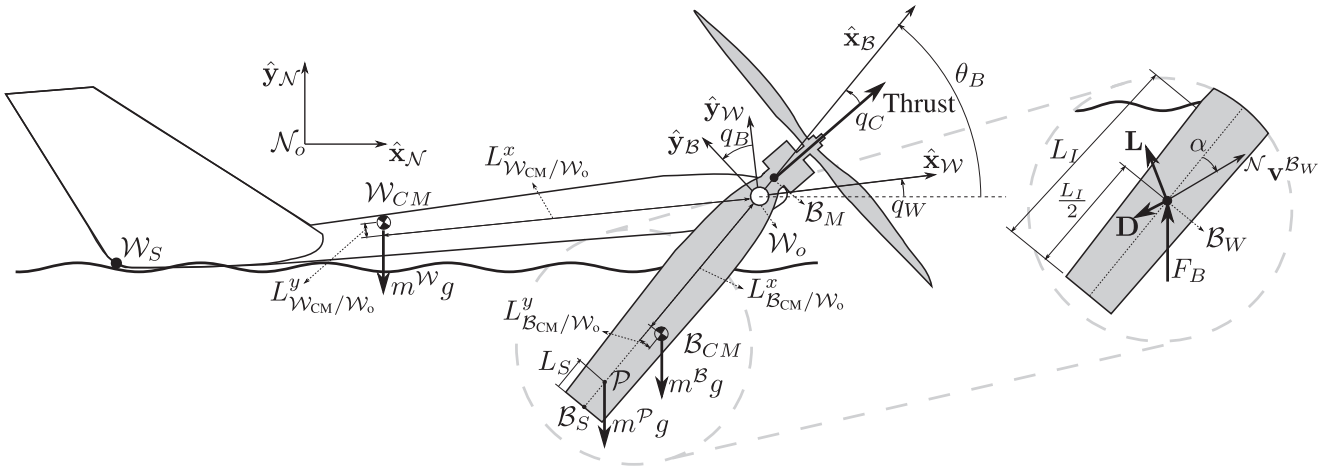

Fig. 3. Diagram of the simplified wing ($\mathcal{W}$), center body ($\mathcal{B}$), reference frames and forces included in the dynamic takeoff model.

5) minimize weight, drag and control complexity from the components added to takeoff and land

With regard to these functional requirements, the Sherbrooke University Water-Air VEhicle (SUWAVE) consists of a reconfigurable flying wing made of two moving parts: the wing and a center body (Fig. 2). The center body, containing all the electronics and the motor, is designed to rotate freely about the front of the wing. In flight, both parts are held together by a latch. When the prototype is ready to takeoff, the latch is released. By doing so, the center body pivots under its own weight, while some water seeps in, to reorient the propeller out of the water to a vertical position. The takeoff maneuver occurs passively and requires no control input. Full thrust is applied and the center body emerges from the water, pulling the wing out. Assuming the proper physical characteristics, both parts get aligned within a fraction of a second and automatically latch together into a normal flight configuration. To land, the prototype dives vertically, nose first in the water like a gannet [18], [19].

This paper addresses essential questions regarding the design of such UAV. Section II and III propose a dynamic model of the passive takeoff and righting maneuvers, and the required physical characteristics for proper operation. Section IV presents an impact model used to compute the accelerations and the stresses in the wing during landing. Finally, Section V and attached video present a functional prototype capable of flying, diving, righting itself, taking off and repeating ad infinitum.

II. Dynamics of Passive Takeoff

As mentioned earlier, the success of the takeoff sequence is dependent on many of the physical characteristics of the prototype (e.g., mass properties, motor thrust line). In order to determine which configurations lead to a successful takeoff, a planar dynamic model is developed. As it will be discussed later, a successful takeoff is obtained when the body latches with the wing at a pitch angle between 40 and 60 degrees. The goal of the model is to simulate the dynamics of a proposed design and determine if the takeoff is successful or not.

The developed planar model consists of two rigid bodies: the wing and the center body as illustrated in Fig. 3. A particle is also added to model the water that seeps inside the body. Four variables are used to describe the configuration of the system: x, y, q_W and q_B. These variables respectively represent the position of the pivot and the angles of the wing and center body. Forces applied on the wing include gravity and contact with the water while the forces applied on the center body include gravity, motor thrust, buoyancy and hydrodynamic forces during the motion through the water. Aerodynamics forces are ignored in the takeoff model. They were initially calculated using a flat plate model [4], but found to represent only 5% of the total gravity forces up to latching. D'Alembert's method is used to derive compact equations of motion of this system. The following sections give more details on these steps and on the validation of the model.

A. Motion

As shown in Fig. 3, the model consists of two rigid bodies, the wing and the center body, connected via a frictionless joint. A particle $\mathcal{P}$ represents the water present in the center body. For convenience, a reference frame $\mathcal{W}$ is attached to the wing and is rotated relative to a Newtonian reference frame $\mathcal{N}$ by the angle q_W around the unit vector $\hat{\mathbf{z}}_{\mathcal{N}}$. Similarly, the reference frame $\mathcal{B}$ is fixed on the body and is rotated with respect to $\mathcal{W}$ by the angle q_B about the unit vector $\hat{\mathbf{z}}_{\mathcal{N}}$. The position of the frictionless joint at the origin of the wing ($\mathcal{W}_{\rm o}$) with respect to the origin of the Newtonian reference frame ($\mathbf{r}^{\mathcal{W}_{\rm o}/\mathcal{N}_{\rm o}}$) is expressed as $x\hat{\mathbf{x}}_{\mathcal{N}} + y\hat{\mathbf{y}}_{\mathcal{N}}$. From this point, the position of the centers of mass of the wing ($\mathcal{W}_{\rm CM}$), the body ($\mathcal{B}_{\rm CM}$) and the particle ($\mathcal{P}$) is expressed as:

$$\mathbf{r}^{\mathcal{W}_{\rm CM}/\mathcal{N}_{\rm o}} = \mathbf{r}^{\mathcal{W}_{\rm o}/\mathcal{N}_{\rm o}} - L^x_{\mathcal{W}_{\rm CM}/\mathcal{W}_{\rm o}}\hat{\mathbf{x}}_{\mathcal{W}} + L^y_{\mathcal{W}_{\rm CM}/\mathcal{W}_{\rm o}}\hat{\mathbf{y}}_{\mathcal{W}} \quad (1)$$

$$\mathbf{r}^{\mathcal{B}_{\rm CM}/\mathcal{N}_{\rm o}} = \mathbf{r}^{\mathcal{W}_{\rm o}/\mathcal{N}_{\rm o}} - L^x_{\mathcal{B}_{\rm CM}/\mathcal{W}_{\rm o}}\hat{\mathbf{x}}_{\mathcal{B}} - L^y_{\mathcal{B}_{\rm CM}/\mathcal{W}_{\rm o}}\hat{\mathbf{y}}_{\mathcal{B}} \quad (2)$$

$$\mathbf{r}^{\mathcal{P}/\mathcal{N}_{\rm o}} = \mathbf{r}^{\mathcal{W}_{\rm o}/\mathcal{N}_{\rm o}} - L^x_{\mathcal{P}/\mathcal{W}_{\rm o}}\hat{\mathbf{x}}_{\mathcal{B}} \quad (3)$$

where parameters $L^i_{A/B}$ represent the distances from point A to point B along the unit vector $\hat{\mathbf{i}}$. Details and values representing the prototype are listed in Table I.

TABLE I
PHYSICAL PROPERTIES OF THE BUILT PROTOTYPE

Parameter	Variable	Value
Wing mass	$m^{\mathcal{W}}$	0.263 kg
Wing ($\mathcal{W}$) inertia about $\mathcal{W}_o$	$I^{\mathcal{W}/\mathcal{W}_o}$	0.00284 kg m^2
$\mathcal{W}_{CM}$ position from $\mathcal{W}_o$ along $\hat{\mathbf{x}}_{\mathcal{W}}$	$L^x_{\mathcal{W}_{CM}/\mathcal{W}_o}$	0.202 m
$\mathcal{W}_{CM}$ position from $\mathcal{W}_o$ along $\hat{\mathbf{y}}_{\mathcal{W}}$	$L^y_{\mathcal{W}_{CM}/\mathcal{W}_o}$	0.002 m
Body mass	$m^{\mathcal{B}}$	0.321 kg
Body ($\mathcal{B}$) inertia about $\mathcal{W}_o$	$I^{\mathcal{B}/\mathcal{W}_o}$	0.0021 kg m^2
$\mathcal{B}_{CM}$ position from $\mathcal{W}_o$ along $\hat{\mathbf{x}}_{\mathcal{B}}$	$L^x_{\mathcal{B}_{CM}/\mathcal{W}_o}$	0.049 m
$\mathcal{B}_{CM}$ position from $\mathcal{W}_o$ along $\hat{\mathbf{y}}_{\mathcal{B}}$	$L^y_{\mathcal{B}_{CM}/\mathcal{W}_o}$	-0.007 m
Motor angle from $\hat{\mathbf{x}}_{\mathcal{B}}$ along $\hat{\mathbf{z}}_{\mathcal{N}}$	q_C	-5.12 deg
$\mathcal{B}_M$ position from $\mathcal{W}_o$ along $\hat{\mathbf{x}}_{\mathcal{B}}$	$L_{\mathcal{B}_M/\mathcal{W}_o}$	0.018 m
$\mathcal{B}_S$ position from $\mathcal{W}_o$ along $\hat{\mathbf{x}}_{\mathcal{B}}$	$L_{\mathcal{B}_S/\mathcal{W}_o}$	0.16 m
Water contact damping coefficient	b	3.75 Nsec/m
Water contact spring coefficient	k	890 N/m

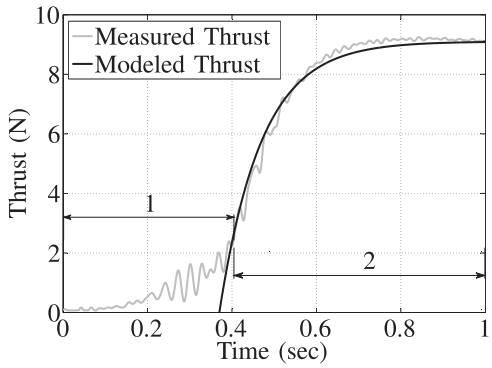

Fig. 4. Measured static thrust as a function of time, filtered with a 12th order zero phase butterworth filter with a cutoff frequency of 8 Hz, and its corresponding first order fit.

B. Forces

The various forces modeled are described below:

1) Gravity: Gravity forces are applied at the center of mass of each body ($m^{\mathcal{W}}g$, $m^{\mathcal{B}}g$ and $m^{\mathcal{P}}g$).

2) Motor Thrust: The motor thrust is applied at point $\mathcal{B}_M$. The thrust line is rotated by an angle q_C about $\hat{\mathbf{z}}_{\mathcal{N}}$ from $\hat{\mathbf{x}}_{\mathcal{B}}$. This variable is important to tune the flight performance and to help the center body clip to the wing during takeoff. The thrust response to a step command was measured with a force sensor (ATI Mini40 SI-20-1) as illustrated in Fig. 4. The initial slope of the measured thrust (Fig. 4, zone 1) corresponds to the open loop initialization sequence of the ESC for the sensorless brushless motor. This part is neglected in the simulation and the remaining response is modeled as a first order step response with a time constant of 0.1 sec. The effect of airspeed is approximated as a negative quadratic function, with the measured static thrust as its maximum and the zero crossing at 20 m/sec. As the prototype velocity attains only 1.75 m/sec up to latching, the variation in thrust remains small.

3) Interaction with Water: The interaction of the wing with water is applied at points $\mathcal{W}_S$ and $\mathcal{W}_o$. The buoyancy forces are calculated from the submerged volume of the front and back halves of the airplane. At point $\mathcal{W}_S$, a viscous force is added in the $\hat{\mathbf{x}}_{\mathcal{N}}$ direction to model the drag created as the submerged section of the wingtip moves through the water during takeoff. This drag force is calculated according to the following equation:

$$F_F = 0.5 C_D \rho A_{\perp} \dot{x}^2_{\mathcal{W}_S} \tag{4}$$

where $A_{\perp}$ corresponds to the component of the submerged wingtip area that is perpendicular to $\hat{\mathbf{x}}_{\mathcal{N}}$, C_D is the drag coefficient of a flat plate perpendicular to the flow (i.e., 2), ρ is the water density, and $\dot{x}_{\mathcal{W}_S}$ is the $\hat{\mathbf{x}}_{\mathcal{N}}$ velocity of point $\mathcal{W}_S$. Both buoyancy and viscous drag forces are set to zero as the points of application leave the surface.

For the center body, the buoyancy force (F_B) is modeled as $\rho g V_D$, where ρ is water density and g is gravity. The displaced volume (V_D) was measured to be 70% of the center body immersed volume. Water fills the rest of the body. Assuming a uniform density and a $\hat{\mathbf{y}}_{\mathcal{B}}$-$\hat{\mathbf{z}}_{\mathcal{B}}$ cross section ($S_{\mathcal{B}}$) of the center body, the buoyancy varies linearly with the immersed length L_I of the body:

$$F_B = 0.7 \rho g S_{\mathcal{B}} L_I \tag{5}$$

This force is exerted on point $\mathcal{B}_W$. This point is located halfway through the immersed length and thus varies as the center body emerges from water (Fig. 3).

4) Lift and Drag: For the Reynolds number (i.e. 100,000) implied in the underwater motion of the center body, a flat plate model adequately approximates the lift $\mathbf{L}$ and drag $\mathbf{D}$ forces as follows [4]:

$$\mathbf{L} = \rho A_{\mathcal{B}} \sin(\alpha)\cos(\alpha) |^{\mathcal{N}}\mathbf{v}^{\mathcal{B}_W}| (\hat{\mathbf{z}}_{\mathcal{B}} \times {}^{\mathcal{N}}\mathbf{v}^{\mathcal{B}_W}) \tag{6}$$

$$\mathbf{D} = -\rho A_{\mathcal{B}} \sin^2(\alpha) |^{\mathcal{N}}\mathbf{v}^{\mathcal{B}_W}| {}^{\mathcal{N}}\mathbf{v}^{\mathcal{B}_W} \tag{7}$$

where ρ is the water density, $A_{\mathcal{B}}$ is the center body area, as projected on the plane normal to $\hat{\mathbf{y}}_{\mathcal{B}}$ (Fig. 3), α is the angle between $\mathcal{B}_W$'s velocity in $\mathcal{N}$ and the center body longitudinal axis ($\hat{\mathbf{x}}_{\mathcal{B}}$) around $-\hat{\mathbf{z}}_{\mathcal{N}}$. The drag is in a direction opposing $\mathcal{B}_W$'s velocity while the lift is perpendicular, in the positive cross product direction. For simplicity, the point of application of both forces is approximated as point $\mathcal{B}_W$.

5) Added Water: The center body is designed to let water seep inside to enable reorientation by sinking. However, the water takes a certain time to drain during takeoff. This phenomenon is represented in the model by adding a particle $\mathcal{P}$ with representative mass and position. This added mass $m^{\mathcal{P}}$ initially corresponds to 30% of the overall body volume filled with water (i.e., 0.14 kg), as discussed earlier. The mass is approximated to decrease linearly from its initial value to zero in 0.65 seconds, as observed experimentally under a acceleration of 1 g, which is comparable to the peak vertical acceleration of 0.7 g measured during takeoff. During that same period, the particle's position $\mathcal{P}$ is varied linearly from the half body length to the end of the center body.

6) Latching: For simplicity, the latch at point $\mathcal{B}_S$ is modeled as a spring-damper ($k = 100$ N/m, $b = 100$ Nsec/m) system that becomes active when q_B is less than 2 degrees. The spring value is chosen to limit the displacement to less than 0.2 deg after latching while the damper value is chosen to prevent rebound.

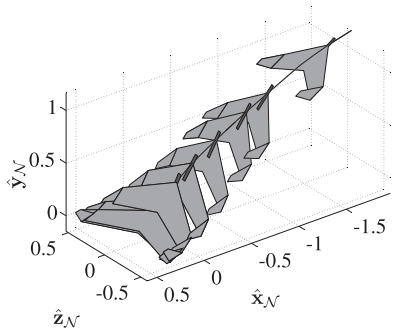

Fig. 5. The 3D trajectory of the prototype during takeoff as captured by Vicon is mostly planar. Frames are spaced by 0.12 sec.

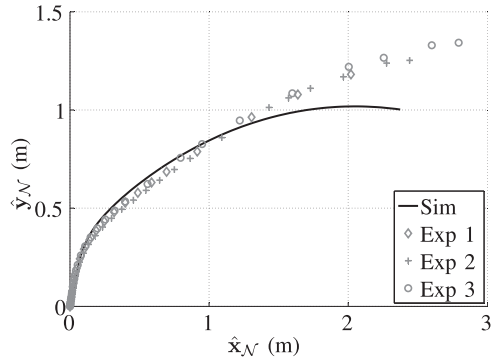

Fig. 6. Comparison of the trajectory of point $\mathcal{W}_o$ in simulation and during three distinct experimental takeoffs for time varying from 0 to 1 sec.

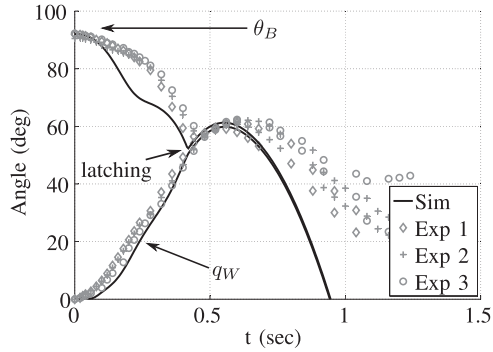

Fig. 7. Time behavior of angles q_W and θ_B. Note that the bracket latches with the wing around $t = 0.4$ sec.

C. Equation of Motion (EOM)

In order to obtain the EOM of the system for the state variables x, y, q_W and q_B, d'Alembert's method is applied. For a system $\mathcal{S}$ of bodies and particles, the resultant forces $\mathbf{F}^{\mathcal{S}}$ and moments $\mathbf{M}^{\mathcal{S}/\mathcal{W}_o}$ about $\mathcal{W}_o$ equal the corresponding effective forces ${}^{\mathcal{N}}\mathbf{F}^{\mathcal{S}}$ and moments ${}^{\mathcal{N}}\mathbf{M}^{\mathcal{S}/\mathcal{W}_o}$ [20]. Thus :

$$\mathbf{F}^{\mathcal{W}+\mathcal{B}+\mathcal{P}} = m^{\mathcal{W}} * {}^{\mathcal{N}}\mathbf{a}^{\mathcal{W}_{\mathrm{CM}}} + m^{\mathcal{B}} * {}^{\mathcal{N}}\mathbf{a}^{\mathcal{B}_{\mathrm{CM}}} + \ldots \\ m^{\mathcal{P}} * {}^{\mathcal{N}}\mathbf{a}^{\mathcal{P}} \quad (8)$$

$$\mathbf{M}^{(\mathcal{W}+\mathcal{B}+\mathcal{P})/\mathcal{W}_o} = {}^{\mathcal{N}}\mathbf{M}^{\mathcal{W}/\mathcal{W}_o} + {}^{\mathcal{N}}\mathbf{M}^{\mathcal{B}/\mathcal{W}_o} + \ldots \\ {}^{\mathcal{N}}\mathbf{M}^{\mathcal{P}/\mathcal{W}_o} \quad (9)$$

$$\mathbf{M}^{(\mathcal{B}+\mathcal{P})/\mathcal{W}_o} = {}^{\mathcal{N}}\mathbf{M}^{\mathcal{B}/\mathcal{W}_o} + {}^{\mathcal{N}}\mathbf{M}^{\mathcal{P}/\mathcal{W}_o} \quad (10)$$

where

$${}^{\mathcal{N}}\mathbf{M}^{\mathcal{W}/\mathcal{W}_o} = \underline{\mathbf{I}}^{\mathcal{W}/\mathcal{W}_o} \cdot {}^{\mathcal{N}}\alpha^{\mathcal{W}} + m^{\mathcal{W}}\mathbf{r}^{\mathcal{W}_{\mathrm{CM}}/\mathcal{W}_o} \times {}^{\mathcal{N}}\mathbf{a}^{\mathcal{W}_o}$$
$${}^{\mathcal{N}}\mathbf{M}^{\mathcal{B}/\mathcal{W}_o} = \underline{\mathbf{I}}^{\mathcal{B}/\mathcal{W}_o} \cdot {}^{\mathcal{N}}\alpha^{\mathcal{B}} + m^{\mathcal{B}}\mathbf{r}^{\mathcal{B}_{\mathrm{CM}}/\mathcal{W}_o} \times {}^{\mathcal{N}}\mathbf{a}^{\mathcal{W}_o}$$
$${}^{\mathcal{N}}\mathbf{M}^{\mathcal{P}/\mathcal{W}_o} = \mathbf{r}^{\mathcal{P}/\mathcal{W}_o} \times m^{\mathcal{P}}{}^{\mathcal{N}}\mathbf{a}^{\mathcal{P}}$$

The linear accelerations ($\mathbf{a}$) of the various points and the angular accelerations (α) of the various rigid bodies in these equations are obtained by time differentiating the corresponding position and orientation of each point and body in the inertial frame $\mathcal{N}$. Scalar equations are produced by extracting the $\hat{\mathbf{x}}_{\mathcal{N}}$ and $\hat{\mathbf{y}}_{\mathcal{N}}$ components of Eqn. 8 and the $\hat{\mathbf{z}}_{\mathcal{N}}$ component of Eqs. 9 and 10. These equations are generated automatically using MotionGenesis and solved with Matlab.

D. Validation

To validate the model, takeoffs with a physical prototype are conducted. The characteristics of this prototype, described in Section V, are measured and listed in Table I.

To compare the results with the model, the position and angles of the wing and the center body are tracked using Vicon motion capture cameras. As the center body orientation is tracked relative to $\mathcal{N}$, the angle θ_B corresponding to the angle between $\hat{\mathbf{x}}_{\mathcal{B}}$ and $\hat{\mathbf{x}}_{\mathcal{N}}$ is introduced. This angle is related to q_B by the equation $\theta_B = q_W + q_B$ and will be used for comparison with the simulation.

An experimental takeoff trajectory is shown in Fig. 5. Full thrust is applied during takeoff with a constant elevon trim to compensate the roll inducing motor torque. This better reproduces the planar conditions of the simulation and ensures a mostly planar takeoff trajectory. Indeed, the RMS ratio of the $\hat{\mathbf{z}}_{\mathcal{N}}$ linear velocity to the $\hat{\mathbf{x}}_{\mathcal{N}} - \hat{\mathbf{y}}_{\mathcal{N}}$ velocity is smaller than 12% while the rotations around $\hat{\mathbf{x}}_{\mathcal{N}}$ and $\hat{\mathbf{y}}_{\mathcal{N}}$ axis are limited to ± 10 degrees.

The results of the simulation are compared to experimental takeoffs in Fig. 6–7. Fig. 6 shows the trajectory of point $\mathcal{W}_o$ for three experimental takeoffs and for the corresponding dynamic simulation. The time behavior of variables q_W and θ_B is illustrated in Fig. 7. For all these tests, the wing starts flat on the water, with the propeller upward. During takeoff, the wing pitches up and latches with the body around 0.4 sec. After latching, the angle of the system naturally decreases toward zero for normal flight. Although the agreement between the simulation and the experimental results is good, particularly for latching angle prediction, small differences exist. The simulation starts diverging after one second as the speed increases and the aerodynamic forces not included in the simulation become more important. Predicted and measured angles prior to latching also differ due to the added inertia and sloshing from the water within the center body. Future versions of the prototype will be designed to better evacuate the water.

E. Design

It was experimentally observed that successful takeoffs require the latching between the wing and the center body to

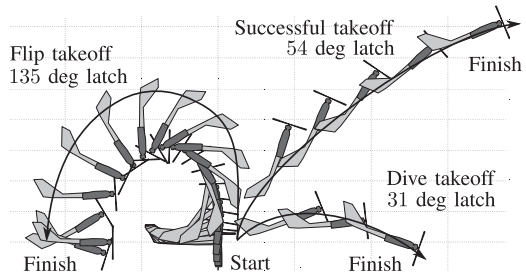

Fig. 8. Simulation of three takeoffs using the parameters of Table I. The value of the motor angle q_C is changed between -0.5 deg (flip) and -9 deg (dive). Both cases latch at an angle outside of the range of 40 to 60 degrees. Refer to Fig. 9 for the acceptable range of q_C.

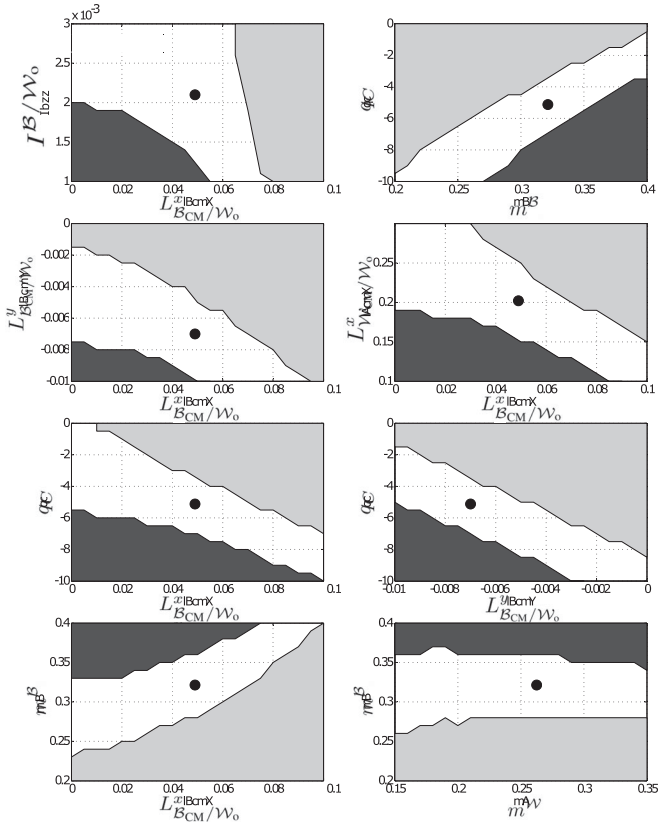

Fig. 9. Influence of each parameters on the success of takeoff. The light gray zone corresponds to a latching angle over 60 degrees while the dark gray zone corresponds to a latching angle below 40 degrees. The white area represents a successful takeoff. Units are expressed in the SI system and degrees. The black dot locates the characteristics of the physical prototype.

occur within a certain range of pitch. Indeed, if latching occurs at a small pitch angle, the front of the prototype usually dives into the water. Similarly, latching at a large pitch angle causes the prototype to flip backward and crash. Both of these scenarios are illustrated in Fig. 8. To determine the influence of the various design parameters one to another, several simulations with varying pairs of parameters were realized. The takeoff were considered as successful when the center body latches with the wing at a pitch angle between 40 and 60 degrees.

From this criterion, Fig. 9 shows the results of the simulations for each pair of parameters. A successful takeoff occurs for pairs

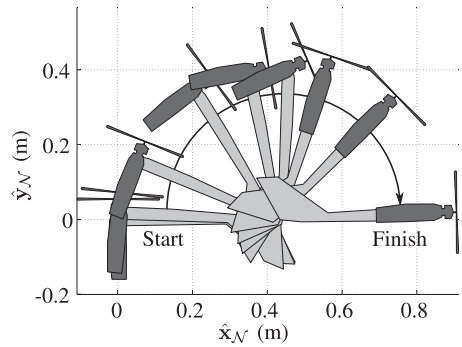

Fig. 10. Simulation results of the wing righting. Refer to supplementary material to see experimental results.

of parameters located within the white area of the graphs. From these graphs, the influence of each parameter is demonstrated and tendencies can be expressed. In general, a negative moment around $\hat{\mathbf{z}}_{\mathcal{B}}$ must be created on the center body to make it latch. However, too much moment will make the wing dive. More negative values of q_C and $L^{y}_{\mathcal{B}_{\mathrm{CM}}/\mathcal{W}_{\mathrm{o}}}$, increasing m^{B}, or decreasing $I^{\mathcal{B}/\mathcal{W}_{\mathrm{o}}}$ and $L^{x}_{\mathcal{B}_{\mathrm{CM}}/\mathcal{W}_{\mathrm{o}}}$ all create a larger negative moment. The results also show that most parameters are linked together. For instance, if $m^{\mathcal{B}}$ is increased, the absolute value of q_C should be more negative to ensure a successful takeoff. Some parameters (e.g., $m^{\mathcal{W}}$), however, have limited impact on the takeoff, as it is shown by the horizontal white area in the bottom-right graph.

III. Righting After Capsize

Interestingly, optimizing the system for successful takeoff also improves the ability of the prototype to right itself in the unlikely chance of capsizing. Indeed, adjusting the parameters for successful right-side up takeoff encourages late latching when taking off from a capsized position and thus flipping. Fig. 10 shows a simulated example of the righting process using the same takeoff model presented in Section II. The thrust is cut when the wing is vertical to ensure a smooth landing.

IV. Dive Landing

As described before, diving is investigated as a preferred method for vertical landing. This landing strategy reduces the approach distance and increases the landing precision, allowing the use of smaller lakes surrounded by tall obstacles. This method also eliminates the approach phase in close proximity to the water during landing, which makes the prototype less sensitive to being capsized by wind gusts or waves. However, this type of landing is still uncommon and the impact forces and resulting structural stresses must be considered.

A. Impact Modeling

To estimate the magnitude of the forces exerted on the wing during landing, experimental dive tests are first conducted. A prototype wing is released from various heights in the water. It is guided along its descent by wires to ensure vertical trajectories with zero angle of attack. The wing is fitted with a GCDC X250-2 accelerometer (3 axes, 14 bits resolution, $\pm$250 g,

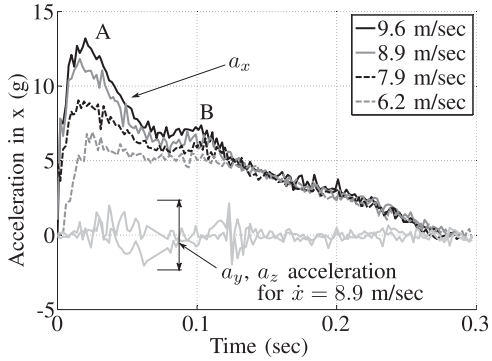

Fig. 11. Measured x accelerations for various impact velocities. The accelerations in y and z are illustrated to show that the impact occurs mainly in x.

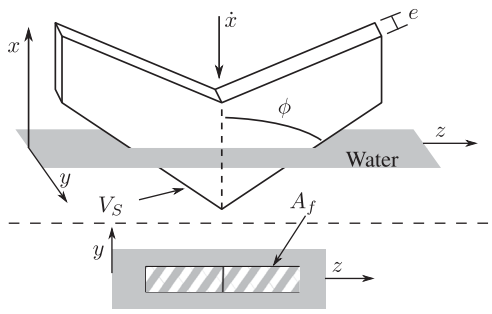

Fig. 12. Representation of the simplified wing, notice the submerged volume and the frontal area

512 Hz). Fig. 11 presents the registered acceleration for different impact velocities. Off axis (i.e., x, y) accelerations are shown to be around 15% of the maximal z acceleration. Dives with negligible angle of attack reduce the total acceleration and a simple flight controller can ensure that this condition is satisfied.

The recorded accelerations show two behaviors: a high peak acceleration (point **A**) varying with the impact velocity and a mostly constant plateau around point **B**. To model the behavior of the wing during its dive, a one dimensional model is used with both a velocity dependent term [21], a submerged volume term and gravity:

$$m\ddot{x} = C_B \rho g V_S + C_V A_f \dot{x}^2 - mg \tag{11}$$

where C_B and C_V are constant coefficients related to the submerged volume and the velocity respectively. They include other effects (e.g., added mass, air entrainment) and are fixed for a wing geometry. The parameters ρ, V_S and A_f are the water density, the submerged volume and the frontal area. The wing is modeled as a simple constant thickness prism as illustrated in Fig. 12. The V_S and A_f terms are function of the position x, the thickness of the wing e and the sweep angle ϕ according to $V_S = e\tan(\phi)x^2$ and $A_f = 2e\tan(\phi)x$. These function can be combined with Eqn. 11 as:

$$m\ddot{x} = C_B \rho g e \tan(\phi)x^2 + 2C_V e \tan(\phi)x\dot{x}^2 - mg \tag{12}$$

To identify parameters C_B and C_V, experimental results are compared to the model. Equation 12 can be solved at point **C** in

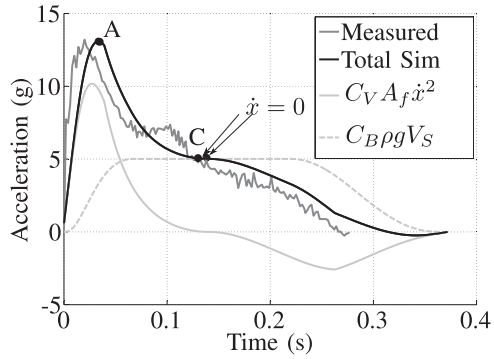

Fig. 13. Impact model as fitted with the experimental results. Individual components of the acceleration are also illustrated ($C_B = 0.6$, $C_V = 50$).

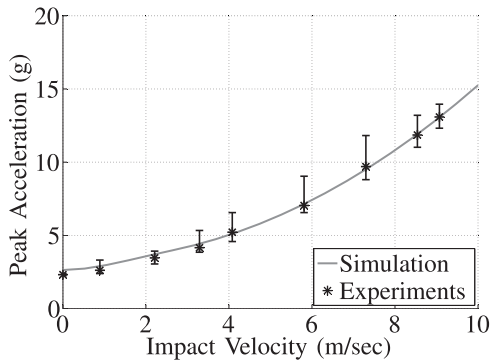

Fig. 14. Graph of peak acceleration vs impact velocity. The parametric model (Eqn. 12, $C_B = 0.6$, $C_V = 50$) is compared with the experimental results. Mean results are represented by the $*$ symbol while the error bars represent the maximum and minimum peak accelerations obtained for five impacts at that velocity.

Fig. 13, where $\dot{x} = 0$ (calculated by integrating the acceleration from the initial impact speed), to find the value of C_B. The value of C_V can then be tuned manually so that the peak of acceleration at point **A** corresponds to the measurements. Fig. 13 shows one experimental dive along with the results of a simulation, including each component of the total acceleration. Fig. 14 shows that the same parameters are valid for a variety of impact speeds, either dominated by buoyancy or velocity related effects. This correlation suggests that impact forces of future geometry could be predicted with a single experimental drop to calibrate C_B and C_V to the platform. Finally, for an impact velocity of 10 m/sec, the maximal depth reached is 0.6 m implying that the prototype could land in shallow water.

B. Structural Sizing

The knowledge of impact acceleration allows the validating of the structural feasibility of a dive landing. The prototype is modeled as a constant section foam beam representing a half wing (Fig. 15). To assume a worst case stress, the carbon fiber spar is not considered in the calculations. The beam is fixed on one end and the accelerations are applied over the wingspan as a uniformly distributed inertial load of magnitude $m\ddot{x}_{\max}/2l$, where $\ddot{x}_{\max}$ corresponds to the maximum acceleration during impact. A reaction force is solely applied on the nose of the

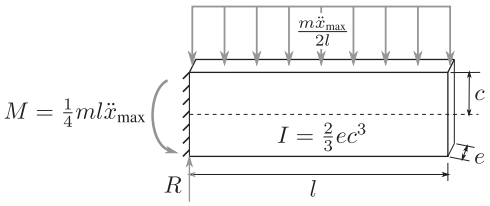

Fig. 15. Representation of a half wing for stress analysis. The equations for the moment and the inertia are expressed as a function of geometry.

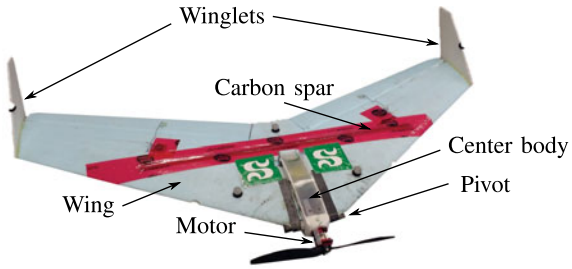

Fig. 16. Representation of the various component of SUWAVE.

prototype (at the fixed end). Overall, this model is conservative as this reaction force is really applied on a broader surface on the wing while most of the mass is located in the center body instead of being uniformly distributed along the wing.

From simple beam theory, the maximum stress σ occurs at the fixture and corresponds to $\sigma = Mc/I$. By replacing the moment M and the inertia I by their values, the stress becomes:

$$\sigma_{\max} = \frac{3ml\ddot{x}_{\max}}{8ec^2} \tag{13}$$

The resistance of the polystyrene foam was estimated at 0.21 MPa [22]. For an impact at 10 m/sec, which corresponds roughly to the cruising speed of the prototype, the peak acceleration is 15 g. This produces a stress of 0.02 MPa, resulting in a margin of safety of 10. Based on the results, it appears that the small frontal area, the profiled shape of the wing and the stiff wing geometry are all contributing to make diving a structurally safe way of landing. As validated on the prototype, this method does not necessitate adding reinforcements, supplementary structure elements or wing folding.

V. Implementation and Results

Using the takeoff dynamic model and XFLR5 [23], a physical configuration was chosen for passive takeoff and stable flight. SUWAVE is a flying wing (Fig. 16) made of polystyrene reinforced with a carbon fiber spar. Two winglets also made of polystyrene are fixed at each end. Beside their normal use in flight, the winglets also keep the wing facing upwind and ready for takeoff while resting on the water. The underside of the wing lays directly in contact with the water so that it remains unperturbed by wind gusts.

The prototype uses a single brushless motor with a 11×6 folding propeller, an 18 A ESC and a 3C 1000 mAh LiPo battery. A receiver and two servomotors control the elevons. A NACA

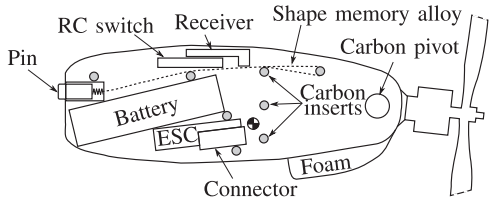

Fig. 17. Cutaway view of the center body. The position of the center of mass is shown.

TABLE II
Mass Budget of the Prototype

Number	Component	Mass (g)
1	Foam wing + carbon spar + winglets	231
2	Carbon pivot + wing latch	14
3	2 GS-9018 servos	18
	Subtotal: Wing	**263**
4	Turnigy 11.1 V 3C 1000 mAh Battery	85
5	Turnigy Plush 18 A ESC	29
6	Spektrum AR610 Receiver	26
7	EMax CF2822 Motor	39
8	11×6 folding propeller	38
9	RC switch + SMA wire + pin	11
10	Battery connector	9
11	Foam	3
12	PLA printed body + carbon inserts	82
	Subtotal: Center body	**321**
	Total weight	**584**

M3 airfoil is chosen for its large thickness ratio, providing space for the electronics. The final design has a 1 m wingspan with a 33 degrees sweep angle. The root chord is 320 mm long with a taper ratio of 0.5.

The center body is made of printed PLA with carbon inserts to hold the components in place and stiffen the structure. A spring loaded pin automatically latches the body with the wing as both bodies become aligned. To release the center body for takeoff, the pin is retracted by a lightweight shape memory alloy wire. A piece of foam added under the center body helps maintaining the propeller upright prior to takeoff. The pivot consists of a carbon tube inserted through the wing and the center body. Fig. 17 presents a cutaway view of the center body while Table II shows a detailed mass budget.

With SUWAVE, numerous takeoff, dive and righting cycles were performed, as illustrated in Fig. 1 and demonstrated in the supplementary video. The prototype performs well but remains sensitive to wind gusts at takeoff, which sometimes prevent the center body from latching.

It is interesting to compare the added mass required by this prototype to that of a quadplane. The components added for takeoff on this prototype (items 2, 9, 10, and 11) weight about 37 g without much optimization. Part of the center body PLA structure should also be added to that total, although the exact fraction is hard to determine because some structural element must be present to support the electronics, even for standard takeoff. The added weight for the presented concept is thus estimated to be between 37 and 119 g. For comparison, converting this flying wing into a quadplane would require the addition of motors, ESC, and fixed propellers

with a combined thrust-to-weight (T/W) ratio larger than one. Assuming components with a similar thrust density as used on this prototype (T/W = 1.56), the added mass of extra motors, ESC and propeller would be between 68 (items 5 and 7) and 106 g (items 5, 7 and 8), without considering the structural elements and wiring of the added propulsion system. The exact number depends on the propeller used. More careful analysis are required, but the concept presented in this paper seems to represent a viable alternative to aquatic quadplanes.

VI. Conclusions and Future Work

This paper presents the modeling, design and fabrication of SUWAVE, a vertical takeoff and landing aquatic UAV. The prototype built is capable of a repeated cycles of flying, diving, righting and takeoff. The takeoff sequence occurs passively and a dynamic model has been developed to serve as a design tool. The influence of relevant parameters such as mass properties and motor angle have been investigated. The prototype is able to self right itself and is robust to wind gusts and waves while floating.

A diving approach has also been investigated for landing and a model predicting the accelerations for various impact velocities has been developed. This model is valid for various impact velocities, can be calibrated quickly from a single dive experiment and provide load cases for the structural design of the wing. By using the geometry of the wing advantageously, diving enables landing in small lakes surrounded by tall obstacles, without the need of reinforcements or wing folding.

The next steps will involve detail optimization and FEA analysis of the airframe to better characterize the additional mass required by this concept. Autonomous mission control will also be implemented for long duration operation and standby. Finally, solar panels will also be added on the wing to allow long endurance missions and lake-to-lake travel.

References

[1] A. Noth, R. Siegwart, and W. Engel, "Design of solar powered airplanes for continuous flight," Ph.D. dissertation, Dept. of Mech. and Process Eng., ETH Zurich, Zurich, Switzerland, 2008.

[2] A. L. Desbiens, A. T. Asbeck, and M. R. Cutkosky, "Landing, perching and taking off from vertical surfaces," *Int. J. Robot. Res.*, vol. 30, no. 3, pp. 355–370, 2011.

[3] M. Kovač, J. Germann, C. Hürzeler, R. Y. Siegwart, and D. Floreano, "A perching mechanism for micro aerial vehicles," *J. Micro-Nano Mechatronics*, vol. 5, no. 3–4, pp. 77–91, 2009.

[4] R. Cory and R. Tedrake, "Experiments in fixed-wing UAV perching," in *Proc. AIAA Guid. Navigat. Control Conf.*, Reston, VA, USA, 2008, pp. 1–12.

[5] G. Xu, Y. Zhang, S. Ji, Y. Cheng, and Y. Tian, "Research on computer vision-based for uav autonomous landing on a ship," *Pattern Recognit. Lett.*, vol. 30, no. 6, pp. 600–605, 2009.

[6] J. Moore and R. Tedrake, "Powerline perching with a fixed-wing UAV," in *Proc. AIAA Infotech@ Aerosp. Conf.*, Seattle, WA, USA, 2009, pp. 1–16.

[7] Natural Resources Canada, "Land and freshwater area, by province and territory," 2005. [Online]. Available: http://www.statcan.gc.ca/tables-tableaux/sum-som/l01/cst01/phys01-eng.htm

[8] MERN Quebec, "Quebec surface hydrography," 2010. [Online]. Available: http://mern.gouv.qc.ca/territoire/portrait/portrait-donnees-mille.jsp

[9] G. Pisanich and S. Morris, "Fielding an amphibious UAV: Development, results, and lessons learned," in *Proc. 21st Digit. Avionics Syst. Conf.*, 2002, vol. 2, pp. 8C4–1.

[10] R. D. Eubank, "Autonomous flight, fault, and energy management of the flying fish solar-powered seaplane," Ph.D. dissertation, Dept. of Aerospace Eng., Michigan Univ., Ann Arbor, MI, USA, 2012.

[11] Univ. Nat. Oceanographic Lab. Syst., "Brief introduction on DRS RQ-15 neptune," 2009. [Online]. Available: http://www.unols.org/sites/default/files/Neptune%20UAV.pdf

[12] Oregon Iron Works, "Sea scout unmanned tactical seaplane offersincreased mission flexibility and utility," 2006.

[13] R. Siddall and M. Kovač, "Launching the aquamav: Bioinspired design for aerial–aquatic robotic platforms," *Bioinspiration Biomimetics*, vol. 9, no. 3, 2014, Art. no. 031001.

[14] M. Schwarzbach, M. Laiacker, M. Mulero-Pázmány, and K. Kondak, "Remote water sampling using flying robots," in *Proc. 2014 Int. Conf. Unmanned Aircr. Syst.*, 2014, pp. 72–76.

[15] P. L. Drews, A. A. Neto, and M. F. Campos, "Hybrid unmanned aerial underwater vehicle: Modeling and simulation," in *Proc. 2014 IEEE/RSJ Int. Conf. Intell. Robots Syst.*, 2014, pp. 4637–4642.

[16] J.-P. Ore, S. Elbaum, A. Burgin, and C. Detweiler, "Autonomous aerial water sampling," *J. Field Robot.*, vol. 32, no. 8, pp. 1095–1113, 2015.

[17] Oakland Univ., Embedded Syst. Res. Lab, "Loon copter.," 2016. [Online]. Available: https://sites.google.com/a/oakland.edu/oar/

[18] J. Liang *et al.*, "Wing load investigation of the plunge-diving locomotion of a gannet Morus inspired submersible aircraft," *Sci. China Technol. Sci.*, vol. 57, no. 2, pp. 390–402, 2014.

[19] X. Yang, J. Liang, T. Wang, G. Yao, W. Zhao, and Q. Shen, "Submersible unmanned aerial vehicle concept design study," in *Proc. Aviation Technol. Integr. Oper. Conf.*, 2013, Paper 4422.

[20] P. Mitiguy, *Advanced Dynamics & Motion Simulation*, Sunnyvale, CA, USA: Prodigy Press, 2014, p. 326.

[21] T. Von Karman, *The Impact on Seaplane Floats During Landing.* Washington, DC, USA: Nat. Advisory Committee Aeronaut., 1929.

[22] The DOW Chemical Company, "Styrofoam polystyrene foam insulation.", 2016. [Online]. Available: http://www.dow.com/elibrary

[23] XFLR5, 2016. [Online]. Available: http://www.xflr5.com/